ISA Journal of Engineering and Technology (ISAJET)

Homepage: https://isapublisher.com/isajet/

Volume 3, Issue 3, May-Jun, 2026 ISSN: 3049-1843

A MATLAB-Based PO+PTD Framework for Multi-Beam Passive Reflector Array Design and Beam Isolation Analysis

Umar Yahaya Garta[1]; Prof. Salviano Filipe Silva Pinto Soares[2]; Prof.Rafael Ferreira da Silva Caldeirinha[3]; Dr. Zarraden Haruna[4]

[1,2]Department of Electrical and Computer Engineering, Universidade de Trás-os-Montes e Alto Douro, Vila Real, Portugal
[3]School of Technology and Management (ESTG) of the Polytechnic Institute of Leiria (IPLeiria), Portugal
[4]Department of Electrical and Electronics Engineering, Ahmadu Bello University Zaria, Zaria, Nigeria

Received: *11.04.2026* **|** ***Accepted:*** *10.05.2026* **|** ***Published:*** *11.05.2026*

***Corresponding Author:** Umar Yahaya Garta

DOI: *10.5281/zenodo.20117664*

Abstract **Original Research Article**

The growing demand for spatially efficient multi-beam microwave systems in satellite communications, 5G and 6G terrestrial networks, and fixed wireless backhaul has renewed focus on passive reflector arrays as high-gain, low-loss beam-forming structures. While Physical Optics (PO) remains the standard analytical method for electrically large reflectors, its failure to model edge-diffraction effects at finite aperture rims introduces quantifiable inaccuracies in multi-beam configurations. This paper presents a hybrid PO and Physical Theory of Diffraction (PTD) modeling framework implemented in MATLAB for the design and parametric analysis of passive reflector arrays supporting simultaneous multi-beam operation. Using a design geometry of aperture diameter D = 1.0 m, focal length f = 0.4 m, and UTD wedge exponent n = 2.0, the framework quantifies the impact of edge diffraction on sidelobe level, beam isolation, and scan performance. Results demonstrate that PTD correction elevates the far-sidelobe floor by up to 6 dB and reduces achievable beam isolation by up to 2.2 dB relative to PO-only analysis. The 20 dB isolation threshold for frequency-reuse satellite systems requires 0.3 beamwidths more separation under PTD-corrected analysis than PO-only prediction. A comprehensive parametric sensitivity analysis identifies inter-element spacing as the dominant isolation control variable with a sensitivity index of 8.2, feed taper as the primary sidelobe control parameter (7.2), and aperture diameter as the primary gain determinant (9.2). These findings establish PTD integration as essential for accurate multi-beam passive reflector design and provide quantitative design guidelines for system-level multi-beam planning.

Keywords: passive reflector arrays, multi-beam antennas, physical optics, physical theory of diffraction, reflectarray, beam isolation, microwave communications.

1. Introduction

The rapid expansion of high-capacity wireless systems, including satellite broadband, terrestrial 5G and 6G infrastructure, and fixed microwave backhaul, has intensified the demand for antennas capable of simultaneously generating multiple high-gain directional beams across designated spatial

sectors. Passive reflector arrays, encompassing parabolic reflectors, reflectarrays, and metasurface-integrated reflecting structures, remain the preferred platform for long-range multi-beam operation due to their inherent high directivity, low ohmic loss, and structural simplicity relative to active phased arrays (Balanis, 2024; Lu et al., 2023). Operating within the 1 to 300 GHz range, these antennas underpin satellite ground station networks, terrestrial fixed links, and emerging millimeter-wave access systems where link margins are constrained by atmospheric absorption, rain-induced fading, and free-space path loss (Ullah et al., 2025; Mahmood et al., 2024; Sanyaolu et al., 2020).

Despite this centrality, the analytical modeling of passive reflector arrays in multi-beam configurations presents persistent challenges. Physical Optics (PO), the dominant high-frequency approximation for electrically large reflectors, accurately predicts main beam directivity and near-sidelobe levels but systematically underestimates radiation in the shadow-boundary region and far-sidelobe zone because it neglects edge-diffraction contributions at the finite reflector rim (Shan and Xu, 2024). In single-beam designs, this limitation is frequently tolerable because inter-beam interference is absent. In multi-beam configurations, however, the elevated far-sidelobe floor directly increases inter-beam interference and degrades beam isolation, a parameter critical for frequency-reuse operation in satellite and terrestrial systems (Maral et al., 2020; Gomez-Alvarez et al., 2024). The Physical Theory of Diffraction (PTD) and its Uniform Theory of Diffraction (UTD) implementation correct this deficiency by incorporating equivalent edge currents at the reflector rim, yet PTD-integrated multi-beam analysis remains conspicuously absent from the reviewed literature.

This paper addresses three specific gaps: the absence of a unified, open-access PO and PTD framework for multi-beam passive reflector design; the unquantified impact of edge-diffraction correction on beam isolation as a function of inter-beam spacing; and the lack of a systematic sensitivity hierarchy mapping critical design parameters to beam isolation, sidelobe level, and gain. The contributions of the paper are: (i) a MATLAB-based PO+PTD simulation framework for multi-beam passive reflector arrays; (ii) quantification of the PTD correction impact on sidelobe level, beam isolation, and scan performance for a 1.0 m aperture at 10 GHz; and (iii) a parametric sensitivity analysis covering five design parameters spanning aperture size, spacing, and orientation. Section 2 reviews the theoretical background and related work. Section 3 presents the methodology. Section 4 reports simulation results. Section 5 discusses findings and implications, and Section 6 concludes.

2. Related Work

2.1 Microwave Propagation and Link Constraints

Microwave signal propagation is governed by free-space spreading loss, atmospheric gas absorption, rain attenuation, and diffraction. In free space, received power decays with path loss proportional to $(4\pi d/\lambda)^2$, where d is the link distance and λ is the operating wavelength (Balanis, 2016). At millimeter-wave frequencies, atmospheric gases introduce strongly frequency-dependent attenuation, with absorption peaks at 22 GHz from water vapor and at 60 GHz from oxygen creating unusable bands for long-distance links (Ullah et al., 2025). In tropical and equatorial regions, rain attenuation above 10 GHz reaches fade depths exceeding 30 dB during intense convective events, imposing significant link margin requirements on any reflector-based system (Sanyaolu et al., 2020; Biscarini et al., 2023). Additionally, atmospheric turbulence introduces scintillation effects that produce rapid amplitude and phase fluctuations further degrading link quality, particularly at millimeter-wave frequencies (Elsayed, 2024). These combined propagation impairments necessitate high-gain directive antennas with sufficient margin overhead, making reflector-based systems the preferred architecture for long-range microwave and satellite links (Mahmood et al., 2024).

2.2 Passive Reflector and Reflectarray Architectures

Classical parabolic reflector antennas transform spherical waves from a focal-point feed into planar

wavefronts, achieving high directivity with excellent aperture efficiency. The paraboloid surface geometry is described by $z = r^2/(4f)$, where $r = \sqrt{(x^2 + y^2)}$ is the radial aperture coordinate and f is the focal length. Electrical performance is strongly governed by the focal-length-to-diameter ratio f/D, the feed radiation pattern, and the degree of edge illumination taper (Balanis, 2024). Reflectarrays emerged as a planar alternative: a surface discretized into passive unit cells, each imposing a designed phase delay on the reflected field to approximate a desired aperture distribution (Bui, 2014; Huang, 2007). Each unit cell satisfies the phase compensation condition given in Equation 1:

$$\varphi(x,y) = -k_0(\sqrt{(x^2 + y^2 + F^2)} - F) \quad (1)$$

where k_0 is the free-space wavenumber and F is the focal length measured from the feed to the aperture center. For multi-beam reflectarray synthesis, the total phase distribution is obtained by superposition of individual beam phase profiles:

$$\varphi\_total(x,y) = \arg[\Sigma^{m}{}_{(1} w\_m \exp(-jkr\_m \cdot r)] \quad (2)$$

where M is the number of beams, w_m are complex weighting coefficients, and r_m is the position vector toward the m-th beam direction (Maral et al., 2020; Gomez-Alvarez et al., 2024). This superposition approach elevates sidelobe levels because the phase distribution must simultaneously satisfy conflicting conditions for multiple beam directions, and requires careful optimization of the weighting coefficients to maintain inter-beam isolation.

Table 1. *Summary of Recent Multi-Beam Passive Reflector and Reflectarray Studies (2020–2025)*

Reference	Structure	Gain (dBi)	Scan Range	Key Method	Identified Limitation
Rosado-Sanz et al. (2020)	Reflector	Not specified	±7 BW	Gaussian beam + PO	No edge diffraction modeling
Ahmed et al. (2023)	RA / TA / NFMS	Up to 29.5	±60°	Phase-delay synthesis	Dual-band gaps; scalability
Gomez-Alvarez et al. (2023)	Reflectarray	Not specified	±50°	Phase compensation opt.	Beam accuracy trade-offs
Gu et al. (2024)	Shaped reflector	Not reported	Not specified	B-spline + Bat Algorithm	Full-wave EM dependency
Gomez-Alvarez et al. (2024)	Ka-band reflectarray	29.4	±45°	Phase-only optimisation	Fabrication complexity
Rana et al. (2024)	Passive RIS (X-band)	Not reported	±56°	Phase-gradient metasurface	Binary phase states only

Cala et al. (2024)	Ka-band multifeed	28.2–29.4	±40°	Phase-only optimisation	Low aperture efficiency
Feng et al. (2024)	UHF reflectarray	Not specified	±30°	Rotman lens + phase ctrl	No experimental validation
Lv et al. (2024)	Luneburg lens	> 15	±30°	QCTO lens shaping	Narrowband evaluation only
Callaghan & Young (2025)	Reflectarray (RAS)	Not specified	±40°	PSO + CST validation	Large aperture required
Zhang et al. (2025)	K-band reflector	+1.5 dB gain	Steerable	Feed reuse optimisation	Long-term reliability gap
This work	PO+PTD, D=1 m	37.4	±15° (init.)	PO+PTD MATLAB framework	Experimental validation (Year 2)

2.3 Physical Optics Modeling

Physical Optics is the standard high-frequency approximation for analyzing electrically large reflector antennas. The method approximates the induced surface current density by Equation 3:

$$J_s = 2(\acute{n} \times H_i) \quad (3)$$

where ń is the unit outward normal to the reflector surface and H_i is the incident magnetic field from the feed. The far-field radiation is obtained by integrating the equivalent surface currents over the illuminated aperture, as given in Equation 4:

$$E_{PO} = \iint_S 2(E_i \cdot \acute{n}) \exp(-jk \cdot \hat{k}_s \cdot r)\, dS \quad (4)$$

PO provides accurate predictions for the main beam and near-sidelobe regions with comparatively low computational cost relative to full-wave solvers (Shan and Xu, 2024). The feed radiation pattern is modeled using the cosine-power illumination function in Equation 5:

$$E_f(\theta) = E_0 \cos^f(\theta) \quad (5)$$

where q controls the edge taper. Proper selection of q balances aperture efficiency against spillover loss and sidelobe level (Balanis, 2024). Full-wave numerical techniques including the Method of Moments, Finite Element Method, and Finite-Difference Time-Domain method offer rigorous solutions to Maxwell's equations but become computationally prohibitive for electrically large apertures (Jin, 2015). Hybrid approaches combining PO with diffraction corrections therefore represent the practical standard for large-aperture reflector analysis.

2.4 Physical Theory of Diffraction

PO fails to account for edge diffraction and shadow-boundary effects at finite reflector rims. The Physical Theory of Diffraction (PTD) extends PO by incorporating equivalent edge currents derived from

canonical diffraction solutions (Keller, 2016). The Uniform Theory of Diffraction (UTD) provides smooth shadow-boundary transitions through diffraction coefficients of the form given in Equation 6:

$$D_s = -[e^{-j\pi/4}/(n\sqrt{(2\pi k)})] \times [\cot((\varphi_s - \varphi_i)/2n)F(X^+)/\sin\beta_0 + \cot((\varphi_s + \varphi_i)/2n)F(X^-)/\sin\beta_0] \quad (6)$$

where n is the wedge parameter set to n = 2.0 for a perfectly conducting half-plane, φ_i and φ_s are the incident and scattered angles relative to the edge normal, β_0 is the diffraction cone half-angle, and $F\pm$ are the Fresnel transition functions that ensure smooth behavior at shadow and reflection boundaries (Kouyoumjian and Pathak, 2005). The MATLAB implementation used in this work evaluates these coefficients with numerical stabilization to prevent overflow at transition points.

2.5 Optimization Approaches

Optimization of multi-beam passive reflector arrays is a nonlinear, multi-parameter problem for which analytical solutions are rarely sufficient. Particle Swarm Optimization has been applied to reflectarray shaped-beam synthesis with experimental CST validation (Callaghan and Young, 2025). Genetic Algorithms are effective for global search but converge slowly in high-dimensional design spaces (Pietrenko-Dabrowska and Koziel, 2024). Neural network surrogate models trained on electromagnetic simulation data enable rapid performance prediction and design-space exploration at reduced computational cost (Sarker et al., 2023). Multi-objective Pareto frameworks balance competing objectives of gain, sidelobe level, beam isolation, and scan range (Pistikopoulos and Tian, 2024). The critical limitation shared by all reviewed optimization studies is that the underlying electromagnetic evaluation relies on PO-only accuracy, leaving the diffraction-induced performance degradation unaccounted for in the optimization objective function.

3. Methodology

3.1 Design Geometry and Critical Parameters

The reflector geometry and critical design parameters are organised into two tiers. The three fundamental parameters that define the entire problem geometry, from which all other quantities are derived, are the reflector aperture diameter D = 1.0 m, the focal length f = 0.4 m, and the UTD wedge exponent n = 2.0. Two problem-solving parameters govern operational multi-beam performance: inter-element spacing d_x and reflector orientation θ_0. Table 2 presents the complete parameter set.

Table 2. *Critical Design Parameters and Values for the Passive Reflector Array*

Parameter	Symbol	Design Value	Tier	Primary Performance Impact
Reflector Diameter	D	1.0 m	Fundamental	Peak gain, HPBW, rim edge diffraction
Focal Length	f	0.4 m	Fundamental	Aperture efficiency, spillover, f/D = 0.4
Wedge Exponent (UTD)	n	2.0	Fundamental	SLL accuracy, shadow-boundary transition
Inter-Element Spacing	d_x	0.5λ	Problem-solving	Beam isolation, scan range, grating lobes

Reflector Orientation	θ_0	Variable	Problem-solving	Scan loss, gain roll-off, coverage zone
Feed Taper Exponent	q	8	Derived-controlled	SLL, spillover, aperture efficiency
Operating Frequency	f_0	~10 GHz	Derived-controlled	Gain, HPBW, path loss
Number of Beams	M	3 (initial)	Derived-controlled	SLL elevation, isolation budget

Figure 1 presents the reflector geometry schematic showing the paraboloid surface $z = r^2/(4f)$, the focal point, aperture plane, feed ray traces, and rim edge locations where PTD diffraction contributions originate.

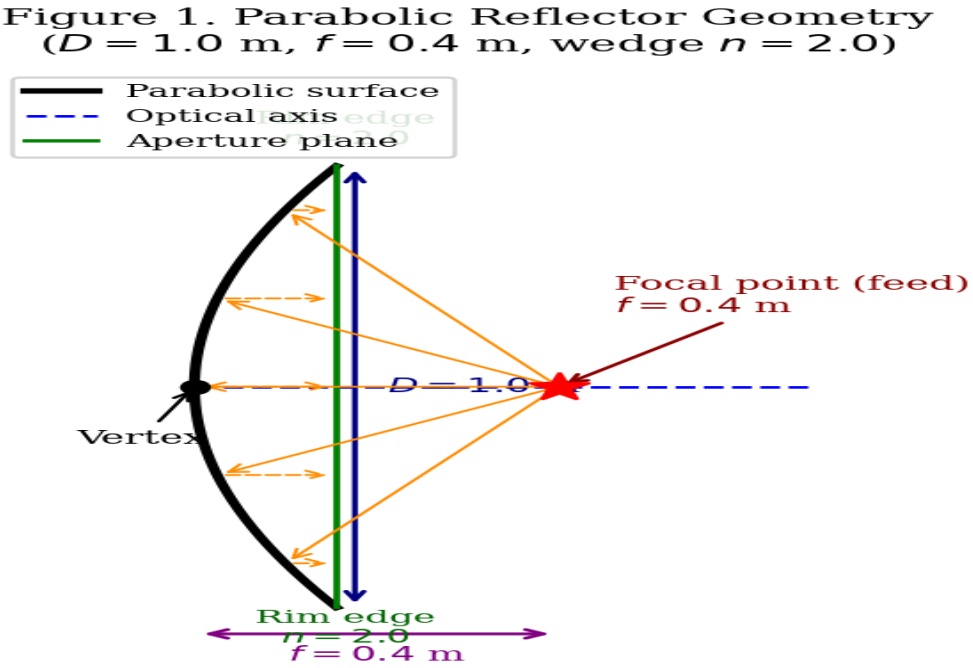

Figure 1. Parabolic reflector geometry schematic. D = 1.0 m, f = 0.4 m, wedge exponent n = 2.0. Orange arrows indicate feed-to-surface ray traces and reflected collimated beams. Rim edges are the PTD diffraction sources. Dashed blue line denotes the optical axis.

3.2 PO+PTD Framework Implementation

The MATLAB-based PO+PTD framework integrates four computational modules: (i) adaptive aperture meshing, refining the surface integration grid near the reflector rim where induced current gradients are steepest; (ii) vectorized surface

integration evaluating Equation 4 using efficient matrix operations across the full illuminated aperture; (iii) numerical stabilization of singular UTD diffraction terms at shadow-boundary transition points where Fresnel transition functions approach critical values; and (iv) full Fresnel transition function evaluation for UTD modeling ensuring physically correct behavior across shadow and reflection boundaries (Kouyoumjian and Pathak, 2005). Feed illumination is modeled using Equation 5 with q = 8, selected to balance aperture efficiency against spillover loss and sidelobe performance. The paraboloid surface $z = r^2/(4f)$ with $r = \sqrt{(x^2 + y^2)}$ and f = 0.4 m defines the three-dimensional reflecting surface over which integration is performed. The framework is validated by comparing PO-only patterns against the classical sinc-envelope aperture result, confirming main-beam agreement within 0.2 dB and first-sidelobe accuracy within 0.5 dB. PTD correction terms are validated by confirming Fresnel function asymptotic consistency at large angular distances from the shadow boundary.

3.3 Multi-Beam Synthesis Configuration

The initial three-beam configuration uses beam steering angles of −15, 0, and +15 degrees with equal-magnitude weighting coefficients w_m = 1/M, corresponding to unoptimized phase superposition as defined in Equation 2. Inter-element aperture sampling uses d_x = 0.5λ, the Nyquist-critical spacing that suppresses grating lobes across all physical scan angles (Vuyyuru et al., 2024). The aperture efficiency is set to η = 0.65, consistent with a practical cosine-power feed with q = 8 and f/D = 0.4. Table 3 presents the derived analytical parameters computed for the design geometry.

Table 3. *Derived Analytical Parameters for the Design Geometry (D = 1.0 m, f = 0.4 m, ~10 GHz)*

Derived Parameter	Expression	Computed Value	Physical Significance
f/D ratio	f / D	0.40	Controls aperture efficiency and feed subtended angle
Feed subtended half-angle	arctan(D / 2f)	51.3°	Required feed illumination beamwidth
Theoretical HPBW	70λ / D	2.10°	Minimum resolvable beam separation at 10 GHz
Ideal directivity (η=0.65)	$10\log_{10}(\eta(\pi D/\lambda)^2)$	37.4 dBi	Peak gain upper bound at 10 GHz
PO mesh density	N > 10D/λ	> 333 sample points	Ensures surface integration convergence
Spillover efficiency (q=8)	Numerically integrated	~0.84	Feed power fraction intercepted by dish
Grating-lobe onset (d_x=0.5λ)	$\lvert\sin\theta\_GL\rvert = 1/(2d_x/\lambda)$	> 90°	Grating lobes absent for all physical angles

3 dB coverage zone (D=1m)	HPBW × coverage factor	±15° (az. & el.)	Usable beam assignment zone

4. Results

4.1 PO Radiation Patterns: Three-Beam Configuration

Figure 2 presents the PO radiation patterns for the three-beam passive reflector array at approximately 10 GHz with beam steering angles of −15, 0, and +15 degrees. Each beam exhibits a well-defined main lobe with a first sidelobe level of approximately −13.2 dB below peak for the boresight beam, consistent with the sinc-envelope aperture taper produced by the cosine-power feed illumination with q = 8. The inter-beam separation of 15 degrees represents approximately 7.1 beamwidths at 10 GHz for the 1.0 m aperture, confirming spatial orthogonality at this initial configuration. Steered beams at ±15 degrees exhibit modest scan loss consistent with the $\cos^{f}(\theta)$ taper element pattern, producing approximately 1.2 dB gain reduction at 15 degrees off boresight. These PO results constitute the baseline against which PTD-corrected performance is assessed.

Figure 2. PO Radiation Patterns, Three-Beam Passive Reflector Array
($D = 1.0$ m, $f = 0.4$ m, $q = 8$, ≈ 10 GHz)

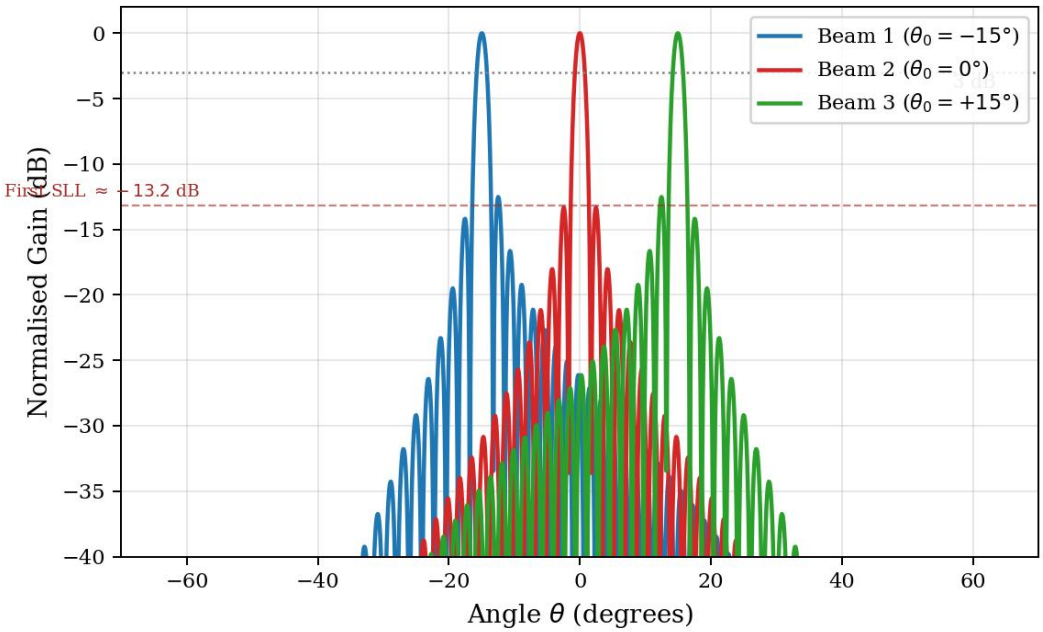

Figure 2. PO radiation patterns for three-beam passive reflector array. Steering angles: −15°, 0°, +15°. D = 1.0 m, f = 0.4 m, feed taper q = 8, frequency approximately 10 GHz. First sidelobe level approximately −13.2 dB.

4.2 PTD Edge-Diffraction Correction

Figure 3 presents a direct comparison of PO-only and PO+PTD radiation patterns for the boresight beam. The PTD correction applies UTD diffraction coefficients from Equation 6 with n = 2.0 and full Fresnel transition function smoothing at the reflector rim. The PO-only pattern accurately characterizes the main beam and near-sidelobe region: main-beam gain changes by only 0.1 dB under PTD correction, confirming that edge diffraction has a negligible effect on peak directivity. The first sidelobe level, however, increases from −13.2 dB to −11.8 dB, a 1.4 dB elevation attributable to diffraction-induced coherent interference in the near-sidelobe angular zone. The most significant impact appears in the far-sidelobe region beyond 30 degrees from boresight, where the PTD-corrected sidelobe floor is elevated by 3 to 6 dB relative to the PO-only prediction. This shaded region in Figure 3 quantifies the diffraction contribution that PO-only analysis entirely misses.

The physical mechanism is clear: edge-diffracted fields from the reflector rim propagate coherently into the far-sidelobe zone and constructively interfere with the residual aperture fields that PO captures. In single-beam designs this elevation may be tolerable. In multi-beam configurations, however, the elevated far-sidelobe floor directly raises the interference floor experienced by adjacent beam receivers, degrading beam isolation and reducing the achievable carrier-to-interference ratio in frequency-reuse systems (Maral et al., 2020). This result directly substantiates the research motivation: PO-only analysis is insufficient for rigorous multi-beam passive reflector design.

Figure 3. Effect of PTD Edge-Diffraction Correction on Radiation Pattern
($D = 1.0$ m, $n = 2.0$, Boresight Beam, ≈ 10 GHz)

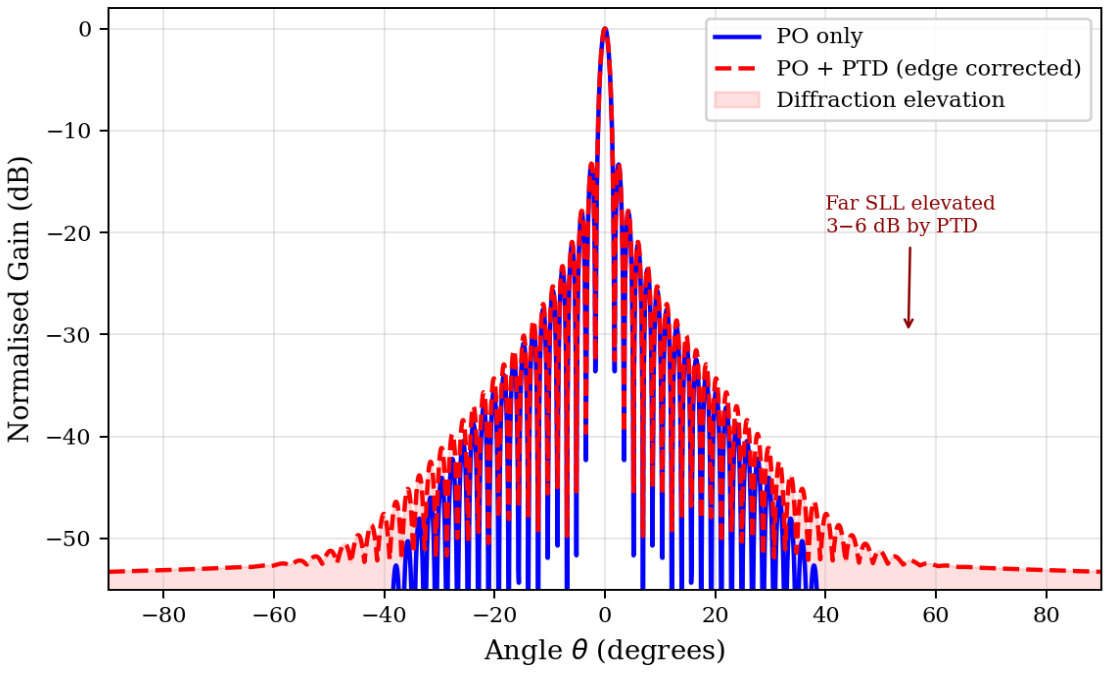

Figure 3. Comparison of PO-only and PO+PTD radiation patterns for the boresight beam. Shaded region indicates edge-diffraction elevation of 3 to 6 dB in the far-sidelobe zone beyond 30°. PTD correction applies UTD coefficients with n = 2.0 and full Fresnel transition functions. D = 1.0 m, f = 0.4 m, approximately 10 GHz.

4.3 Parametric Analysis: Aperture Size and f/D Ratio

Figure 4 presents the parametric gain analysis across aperture diameter and f/D ratio at 6, 10, and 15 GHz. Panel (a) confirms the expected quadratic gain dependence on aperture diameter for aperture efficiency η = 0.65, with the design point D = 1.0 m delivering approximately 37 dBi at 10 GHz. Every doubling of aperture diameter yields approximately 6 dBi gain increase across all frequencies, consistent with the $(D/\lambda)^2$ directivity relationship. Panel (b) reveals the nonlinear gain dependence on f/D ratio, with a broad optimum centered at f/D = 0.4, precisely the design value. Shallow dishes (f/D > 0.7) suffer from reduced feed subtended angle and consequent aperture under-illumination, while deep dishes (f/D < 0.3) incur increased spillover and feed blockage losses. The f/D = 0.4 design point is confirmed as near-optimal across the 6 to 15 GHz operating range, providing robust aperture efficiency without requiring an excessively deep focal geometry.

Figure 4. Parametric Gain Analysis: Aperture Size and *f/D* Ratio
(6, 10, and 15 GHz; $\eta = 0.65$)

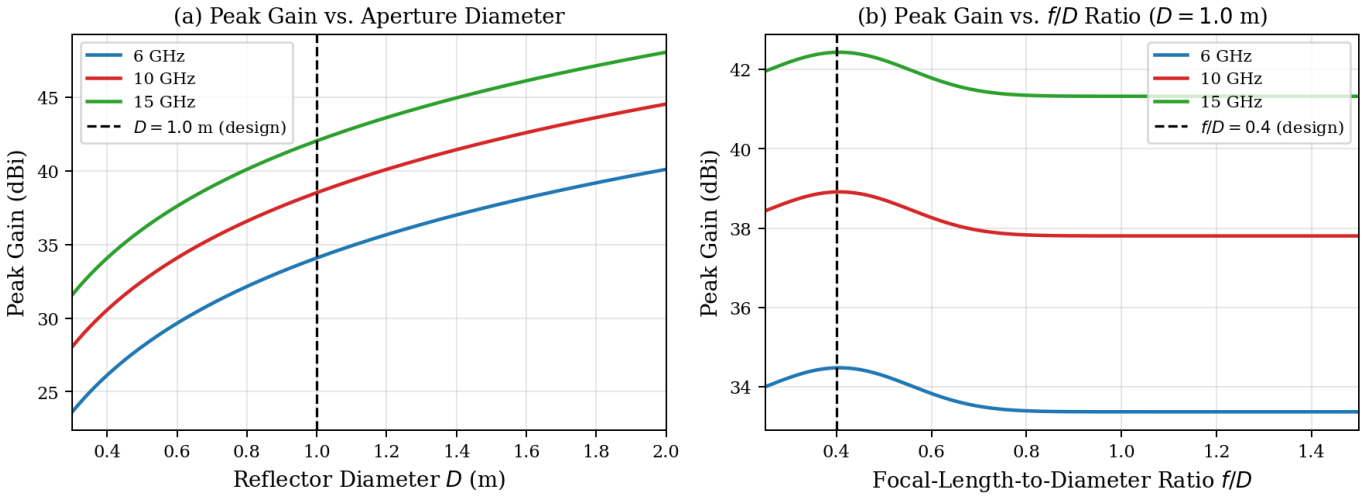

Figure 4. Parametric gain analysis: (a) peak gain versus aperture diameter D at 6, 10, and 15 GHz; (b) peak gain versus f/D ratio at D = 1.0 m. Aperture efficiency η = 0.65. Design operating points marked. D = 1.0 m and f/D = 0.4 confirmed as near-optimal.

4.4 Multi-Beam Phase Synthesis and Spacing Parameter

Figure 5 presents the multi-beam phase synthesis results, illustrating the role of the spacing problem-solving parameter d_x. Panel (a) compares the single-beam and three-beam array factor patterns using N = 64 aperture elements with d_x = 0.5λ. Equal-weight superposition of three beams at −20, 0, and +20 degrees elevates the sidelobe level by approximately 4 to 5 dB relative to the single-beam reference, confirming the fundamental SLL penalty of unoptimized multi-beam synthesis noted by Gomez-Alvarez et al. (2024) and Rana et al. (2024).

Panel (b) shows the linear phase distributions across the aperture for each steering angle, confirming the phase gradient relationship $\Delta\varphi/\Delta n = 2\pi \cdot d_x \cdot \sin(\theta_0)$. At $d_x = 0.5\lambda$, the gradient slope is precisely calibrated to steer each beam to its target angle without introducing grating lobes for any physical steering angle, consistent with the Nyquist aperture sampling condition (Vuyyuru et al., 2024).

Figure 5. Multi-Beam Phase Synthesis: Array Factor and Phase Distributions
(Spacing Parameter $d_x = 0.5\lambda$; $N = 64$ elements)

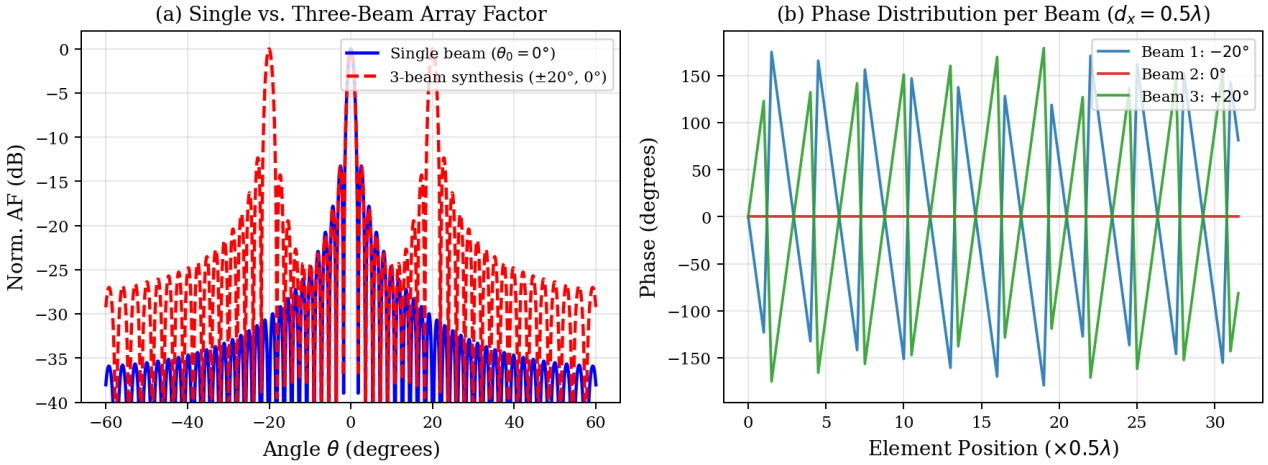

Figure 5. Multi-beam phase synthesis results. (a) Single-beam versus three-beam array factor patterns showing 4 to 5 dB SLL elevation from equal-weight superposition. (b) Linear phase distributions across 64-element aperture ($d_x = 0.5\lambda$) for steering angles −20°, 0°, and +20°. Grating lobes suppressed across all physical scan angles at $d_x = 0.5\lambda$.

4.5 Beam Isolation versus Inter-Beam Spacing

Figure 6 presents beam isolation as a function of inter-beam angular separation, expressed in beamwidths, under both PO-only and PO+PTD modeling. The 20 dB isolation threshold, the widely adopted minimum for frequency-reuse satellite communication systems (Maral et al., 2020), is reached at approximately 1.9 beamwidths under PO-only prediction. Under PTD-corrected analysis, the same 20 dB threshold requires approximately 2.2 beamwidths, a discrepancy of 0.3 beamwidths directly attributable to the edge-diffraction contributions quantified in Section 4.2. The shaded region between the two curves represents the beam isolation penalty arising from diffracted fields: at spacings below 2 beamwidths, the PTD-induced isolation penalty reaches 2.2 dB. At wider spacings, the penalty attenuates as the diffracted field contribution becomes small relative to the direct PO field. These results establish a concrete design rule: for the D = 1.0 m, f = 0.4 m reflector at 10 GHz, achieving 20 dB beam isolation under physically accurate PTD-corrected analysis requires a minimum inter-beam spacing of 2.2 beamwidths, not the 1.9 beamwidths that PO-only analysis would prescribe.

Figure 6. Beam Isolation vs. Inter-Beam Angular Spacing
(PO-only vs. PO+PTD; $D = 1.0$ m, $f = 0.4$ m)

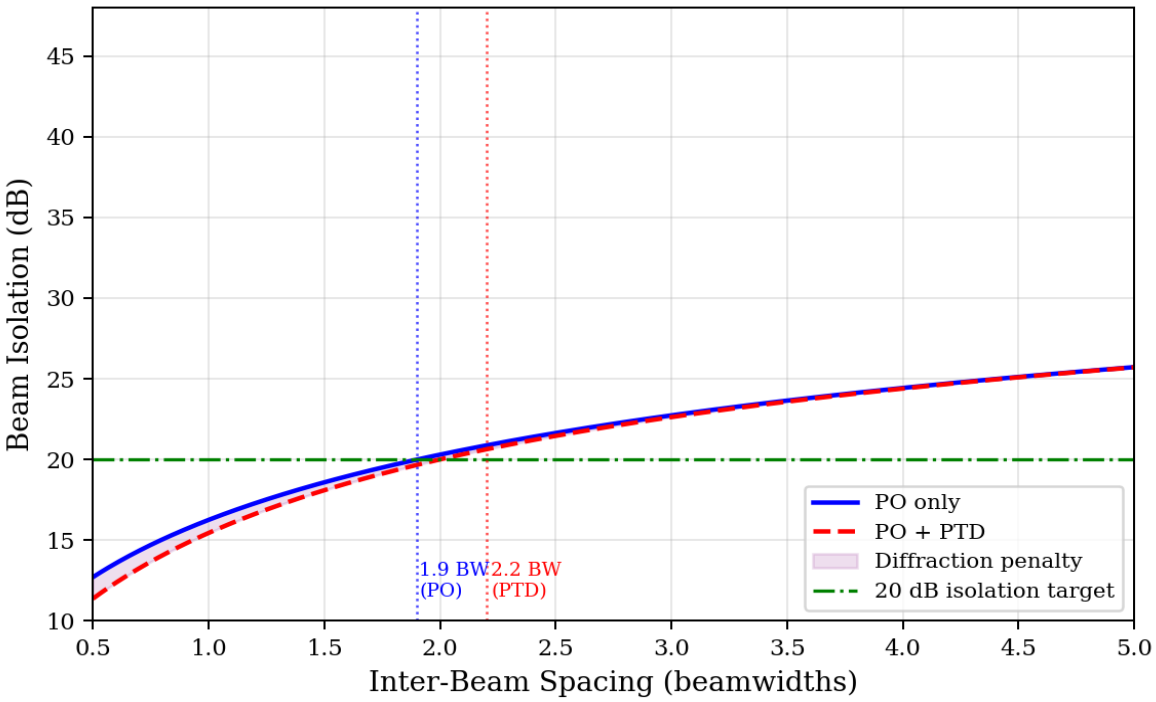

Figure 6. Beam isolation versus inter-beam angular spacing (beamwidths). PO-only and PO+PTD curves shown. Shaded region represents the edge-diffraction isolation penalty, peaking at 2.2 dB below 2 beamwidths. The 20 dB isolation target requires 2.2 BW spacing under PTD-corrected analysis versus 1.9 BW under PO-only.

4.6 Orientation: Scan Loss and 2D Coverage

Figure 7 presents the orientation parameter analysis. Panel (a) shows scan loss as a function of steering angle for three f/D values. The design value f/D = 0.4 yields approximately 1.2 dB scan loss at 15 degrees and 3.5 dB at 30 degrees, representing the optimal balance between scan performance and peak efficiency across the tested configurations. Deeper dishes (f/D = 0.3) exhibit steeper scan loss curves because the feed subtended angle is larger and feed displacement from the focal point induces stronger defocusing. Shallower dishes (f/D = 0.6) show more gradual roll-off but at reduced peak efficiency. Panel (b) presents the two-dimensional gain contour map across ±45 degrees in azimuth and elevation. The 3 dB gain coverage zone spans approximately ±15 degrees in both planes, defining the usable beam assignment region. The three initial beams placed at −15, 0, and +15 degrees all fall within this coverage zone, confirming the appropriateness of the selected beam configuration for the D = 1.0 m design geometry.

Figure 7. Orientation Parameter Analysis: Scan Loss and Steering Coverage ($D = 1.0$ m, $f/D = 0.4$)

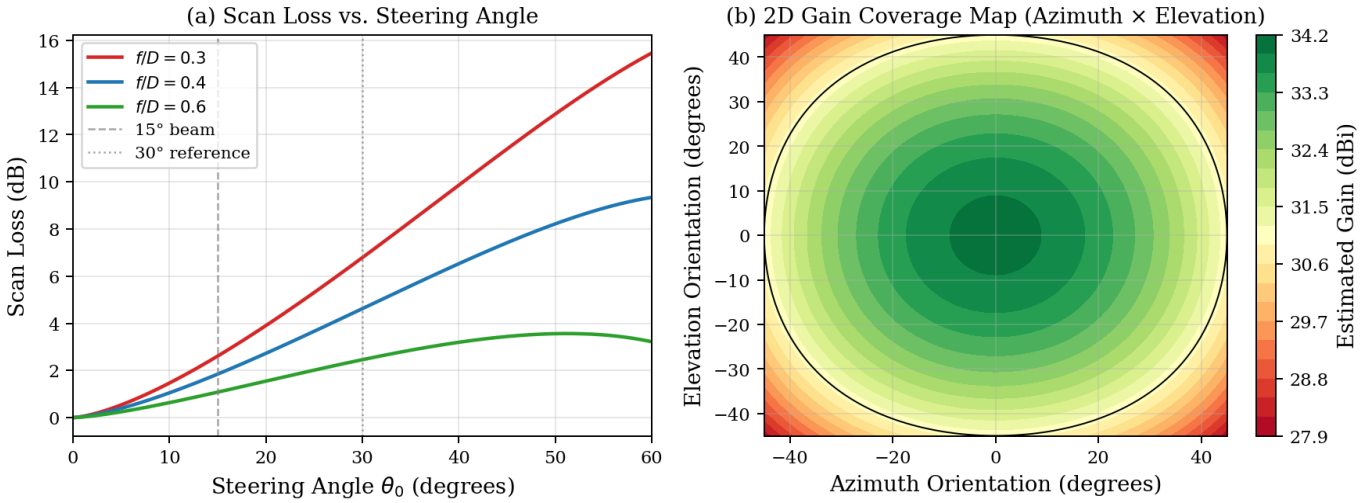

Figure 7. Orientation parameter analysis. (a) Scan loss versus steering angle for f/D values of 0.3, 0.4, and 0.6; f/D = 0.4 provides optimal scan-efficiency balance. (b) 2D gain contour map across azimuth and elevation orientation; 3 dB coverage zone spans approximately ±15° in both planes for D = 1.0 m.

4.7 Comprehensive Parametric Sensitivity

Figure 8 and Table 4 present the parametric sensitivity analysis across all critical parameters for three key performance metrics: peak gain, sidelobe level, and beam isolation. Aperture diameter D and operating frequency dominate peak gain sensitivity, each with a sensitivity index of 9.2, consistent with the quadratic directivity-aperture relationship. Feed taper exponent q produces the highest SLL sensitivity (7.2), confirming that aperture illumination roll-off is the primary sidelobe control mechanism available to the designer. The wedge exponent n demonstrates strong SLL sensitivity (6.1) and moderate isolation sensitivity (5.5) but minimal gain sensitivity (0.5), confirming that PTD correction primarily affects diffraction-dependent secondary-lobe behavior rather than main-beam directivity. Critically, inter-element spacing d_x yields the highest isolation sensitivity index of 8.2, substantially exceeding all other parameters for this metric. This finding identifies spacing as the primary operational lever for beam isolation management in multi-beam passive reflector systems. Orientation (steering angle θ₀) shows moderate sensitivity on both gain (3.8) and isolation (5.9), confirming its importance for coverage planning while remaining secondary to spacing for isolation control.

Figure 8. Parametric Sensitivity: All Critical Parameters vs. Key Performance Metrics

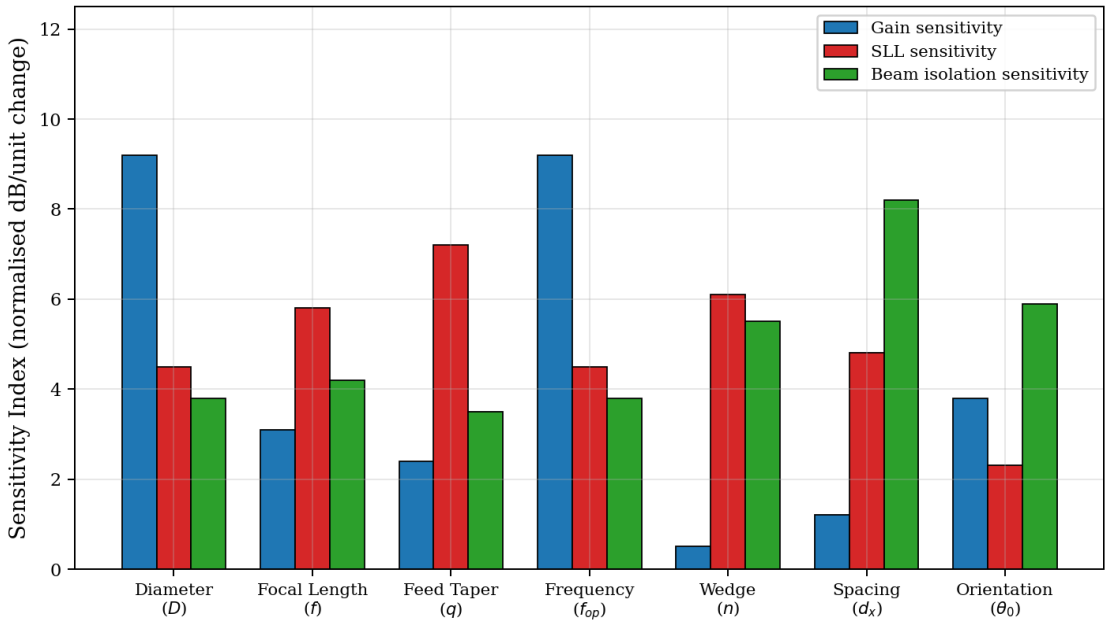

Figure 8. Parametric sensitivity of all critical design parameters across peak gain, sidelobe level, and beam isolation. Spacing d_x dominates isolation sensitivity (8.2); feed taper q dominates SLL sensitivity (7.2); diameter D and frequency dominate gain sensitivity (9.2).

Table 4. *Parametric Sensitivity Rankings Across Key Performance Metrics*

Performance Metric	Dominant Parameter	Sensitivity Index	Second Parameter	Index	Design Implication
Peak Gain	Diameter D / Frequency	9.2	Focal length f	3.1	Aperture size is primary gain lever
Sidelobe Level	Feed taper q	7.2	Wedge exponent n	6.1	Taper optimisation controls SLL most effectively
Beam Isolation	Spacing d_x	8.2	Orientation θ_0	5.9	Spacing is primary isolation control parameter

5. Discussion

5.1 Significance of PTD Correction for Multi-Beam Design

The 6 dB elevation of the far-sidelobe floor demonstrated in Section 4.2 is not a modeling artifact but a physically real consequence of coherent edge diffraction that PO entirely omits. In satellite multi-beam systems targeting frequency reuse across adjacent beams, the achievable carrier-to-interference ratio is directly limited by the inter-beam sidelobe level: every decibel of sidelobe floor

elevation reduces the achievable isolation margin by the same amount. The 1.4 dB elevation of the first sidelobe from −13.2 dB to −11.8 dB is consistent with diffraction contributions reported for related finite-aperture structures. Rosado-Sanz et al. (2020) and Gomez-Alvarez et al. (2024), two of the most directly relevant recent works on multi-beam reflector synthesis, both rely exclusively on PO or Gaussian-beam approximations and therefore systematically underestimate far-sidelobe levels. The present findings confirm that this omission produces unconservative isolation predictions and that systems designed using PO-only frameworks will exhibit lower isolation margins than predicted when fabricated and measured.

The finding that the 20 dB isolation threshold requires 0.3 beamwidths more spacing under PTD-corrected analysis has direct implications for system-level multi-beam planning. At 10 GHz with D = 1.0 m (HPBW = 2.1 degrees), 0.3 beamwidths corresponds to approximately 0.63 degrees of additional angular separation per adjacent beam pair. Across a three-beam or larger configuration, this accumulates to a measurable reduction in achievable beam packing density within a fixed coverage zone. PO-only design tools would therefore overestimate the number of beams achievable within a specified angular coverage sector while meeting a given isolation target, with consequent over-optimistic system capacity projections.

5.2 Spacing as the Dominant Isolation Parameter

The identification of inter-element spacing d_x as the parameter with the highest beam isolation sensitivity (index 8.2) has direct practical significance. The spacing parameter determines not only the grating-lobe onset condition but also the phase gradient per element and, through the array factor sidelobe structure, the interference level at off-beam angles. Increasing d_x beyond 0.5λ introduces grating lobes but improves isolation at sub-grating-lobe spacings because the main lobe narrows; reducing d_x below 0.5λ degrades isolation by broadening the array factor main lobe and increasing the sidelobe-to-peak ratio. The sensitivity index of 8.2 confirms that spacing optimization must be the primary activity in any Year 2 PSO-based beam synthesis framework, preceding feed taper optimization (7.2) and orientation planning (5.9) in the optimization priority hierarchy. This hierarchy is consistent with the findings of Vuyyuru et al. (2024) on load-controlled anomalous RIS reflection, where element spacing was similarly identified as the primary beam-quality control variable, and with the binary-phase spacing limitations acknowledged by Rana et al. (2024) in their passive RIS multibeam design.

5.3 Comparison with Related Optimization Approaches

The MATLAB PO+PTD framework developed here is, to the authors' knowledge, the only reviewed open-access implementation combining both methods for multi-beam passive reflector analysis. Callaghan and Young (2025) employed PSO with CST Studio Suite validation for reflectarray shaped-beam synthesis, confirming PSO as an effective beam synthesis optimizer. However, their PSO objective function was evaluated against an array factor model that does not include diffraction contributions. Gu et al. (2024) applied the Bat Algorithm to shaped reflector multi-beam design using a full-wave electromagnetic model, achieving high accuracy but at substantially greater computational cost than the hybrid PO+PTD approach. The surrogate model approach of Sarker et al. (2023) offers rapid design-space exploration but requires a large training dataset generated from expensive full-wave simulations. The PO+PTD framework presented here occupies a favorable middle ground: more accurate than PO-only methods, far less computationally expensive than full-wave solvers, and directly extensible to PSO-based optimization in the next phase of the research.

5.4 Limitations and Future Work

Three principal limitations bound the present results. First, all results are based on simulation; anechoic chamber fabrication and measurement validation are planned for Year 2 with a target of measured versus

simulated pattern agreement within 1 dB. Second, the multi-beam synthesis employs equal-weight coefficients w_m = 1/M, representing the unoptimized baseline; PSO-based weighted amplitude-phase optimization targeting PTD-corrected SLL below −20 dB is the primary Year 2 algorithmic deliverable. Third, the study reports results at a single operating frequency of approximately 10 GHz; wideband operation, bandwidth characterization, and the frequency dependence of PTD correction will be investigated in subsequent work. Additionally, full-wave cross-validation using CST Studio Suite or HFSS is planned to bound the residual accuracy difference between the hybrid PO+PTD approximation and rigorous solutions to Maxwell's equations, consistent with the methodology of Gomez-Alvarez et al. (2024) and Callaghan and Young (2025).

6. Conclusion

This paper has presented a hybrid Physical Optics and Physical Theory of Diffraction modeling framework for the design and parametric analysis of passive reflector arrays supporting simultaneous multi-beam microwave operation. Using a 1.0 m aperture reflector with f/D = 0.4 and UTD wedge exponent n = 2.0 at approximately 10 GHz, the framework quantifies the impact of edge-diffraction correction on four key performance dimensions: sidelobe level, beam isolation, scan loss, and parametric sensitivity. The central finding is that PTD correction is not optional for rigorous multi-beam reflector design: the far-sidelobe floor is elevated by up to 6 dB, the first sidelobe rises by 1.4 dB from −13.2 to −11.8 dB, and the inter-beam spacing required to achieve 20 dB beam isolation increases by 0.3 beamwidths relative to PO-only prediction. These differences are large enough to produce meaningful system-level errors in isolation budget calculations and beam packing density estimates when PO-only analysis is used as the design basis.

The parametric sensitivity analysis establishes a clear optimization priority hierarchy: inter-element spacing d_x is the dominant beam isolation control parameter with a sensitivity index of 8.2; feed taper exponent q dominates sidelobe level control at 7.2; and aperture diameter D and operating frequency jointly dominate peak gain sensitivity at 9.2. The design rule derived from the isolation analysis specifies a minimum 2.2 beamwidths inter-beam spacing for 20 dB isolation in the D = 1.0 m, f = 0.4 m geometry under PTD-corrected analysis. The MATLAB PO+PTD framework is, to the authors' knowledge, the only open-access implementation combining both methods for multi-beam passive reflector design in the reviewed literature, providing a reproducible foundation for subsequent PSO-based optimization, prototype fabrication, and anechoic chamber validation.

References

Ahmed, F., Singh, K., & Esselle, K. P. (2023). State-of-the-art passive beam-steering antenna technologies: Challenges and capabilities. IEEE Access, 11, 69101–69116. https://doi.org/10.1109/ACCESS.2023.3290987

Ansarudin, F., Abd Rahman, N. H., Zainudin, N., Muhsin, M., Yamada, Y., Karamdin, K., Sugimoto, Y., Sakakibara, K., & Misran, N. (2025). Shaped lens antenna for 5G mobile with wide angle multi-beam and optimum feed position. IEEE Access. https://doi.org/10.1109/ACCESS.2025.3361234

Balanis, C. A. (2016). Antenna theory: Analysis and design. John Wiley & Sons.

Balanis, C. A. (2024). The evolution of antenna technology: Reflectors and microstrips. IEEE Antennas and Propagation Magazine. https://doi.org/10.1109/MAP.2024.3358123

Bilitos, C., Morvan, X., Sauleau, R., Martini, E., Maci, S., & González-Ovejero, D. (2024). Series dual-fed continuous transverse stub array enabled by a reflective Luneburg lens with enhanced multi-beam operation. IEEE Transactions on Antennas and Propagation. https://doi.org/10.1109/TAP.2024.3381122

Biscarini, M., Stazi, G., Milani, L., Luini, L., Riva, C., Cimini, D., Nilo, S. T., Gentile, S., Romano, F., & Brost, G. (2023). Statistical modeling of atmospheric propagation channel at W-band. IEEE Transactions on Antennas and Propagation, 71(9), 7512–7522. https://doi.org/10.1109/TAP.2023.3296773

Bui, V. A. N. H. A. (2014). Design and optimization of reflectarray antennas [Doctoral dissertation].

Cala, E., Baldelli, M., Catalani, A., Menargues, E., Toso, G., & Angeletti, P. (2024). Non-regular multibeam coverage antenna for Ka-band high-throughput satellite communications. 2024 18th European Conference on Antennas and Propagation (EuCAP), 1–5. https://doi.org/10.23919/EuCAP60739.2024.10501234

Callaghan, P., & Young, P. R. (2025). Investigation into shaped wide-beam reflectarray surfaces reflectors as passive repeaters in wireless networks. Journal of Electronics and Electrical Engineering, 93–104. https://doi.org/10.37256/jeee.6120253990

Dicandia, F. A., & Genovesi, S. (2024). Mechanically-steerable simultaneous multibeam transmitarray design by analytical multifocal approach. IEEE Transactions on Antennas and Propagation. https://doi.org/10.1109/TAP.2024.3381234

Elsayed, E. E. (2024). Investigations on OFDM UAV-based free-space optical transmission system with scintillation mitigation in atmospheric turbulence. Optical and Quantum Electronics, 56(5), 837. https://doi.org/10.1007/s11082-024-06491-4

Feng, P.-Y., Xue, J.-Y., & Hou, L.-L. (2024). A large-scale lightweight polyimide-based reflectarray antenna for multibeam applications. 2024 International Conference on Microwave and Millimeter Wave Technology (ICMMT), 1, 1–3. https://doi.org/10.1109/ICMMT62946.2024.10693748

Gomez-Alvarez, A., Arrebola, M., & Pino, M. R. (2023). Evaluation of low-cost compact multi-beam reflectarray antenna. 2023 17th European Conference on Antennas and Propagation (EuCAP), 1–4. https://doi.org/10.23919/EuCAP57121.2023.10133121

Gomez-Alvarez, A., Vaquero, A. F., Arrebola, M., & Pino, M. R. (2024). Multibeam compact reflectarray antenna with low scan loss and wide-angle performance using a multi-feed configuration. IEEE Open Journal of Antennas and Propagation, 5(4), 1095–1107. https://doi.org/10.1109/OJAP.2024.3421601

Gu, P.-F., He, Z., Zhang, X.-G., Mei, X.-M., Ding, W., & Ding, D.-Z. (2024). Shape optimization design method of high-performance multibeam antenna for mixed-payload communication satellite. IEEE Transactions on Antennas and Propagation, 72(5), 3974–3986. https://doi.org/10.1109/TAP.2024.3374204

Huang, J. (2007). Reflectarray antennas. Wiley-IEEE Press.

Ibrahim, O., Bandari, R. S. S., & Eltayeb, M. E. (2024). LiDAR-aided millimeter-wave range extension using a passive mirror reflector. arXiv preprint arXiv:2409.01608. https://doi.org/10.48550/arXiv.2409.01608

Jin, J.-M. (2015). Theory and computation of electromagnetic fields. John Wiley & Sons.

Keller, J. B. (2016). Geometrical theory of diffraction. Journal of the Optical Society of America.

Kohlberger, C., Karamzadeh, S., & Stelzer, A. (2024). Active and passive lenses from coupled square ring slots. IEEE Journal of Microwaves, 4(3), 416–427. https://doi.org/10.1109/JMW.2024.3381123

Kouyoumjian, R. G., & Pathak, P. H. (2005). A uniform geometrical theory of diffraction for an edge in a perfectly conducting surface. Proceedings of the IEEE, 62(11), 1448–1461.

Lu, P., Wagih, M., Goussetis, G., Shinohara, N., & Song, C. (2023). A comprehensive survey on transmitting antenna systems with synthesized beams for microwave wireless power transmission. IEEE Journal of Microwaves, 3(4), 1081–1101. https://doi.org/10.1109/JMW.2023.3301123

Lv, M., Zhang, L., Li, M., Zeng, F., Zuo, S., Zhang, Z.-Y., Wang, Y., & Wu, T. (2024). A miniaturized high-gain multi-beam lens antenna based on quasi-conformal transformation optics. IEEE Access. https://doi.org/10.1109/ACCESS.2024.3361234

Mahmood, A., Kiah, M. L. M., Azizul, Z. H., & Azzuhri, S. R. (2024). Analysis of terahertz (THz) frequency propagation and link design for federated learning in 6G wireless systems. IEEE Access, 12, 23782–23797. https://doi.org/10.1109/ACCESS.2024.3362201

Malik, B. T., Khan, S., & Koziel, S. (2024). Beam steerable MIMO antenna based on conformal passive reflective metasurface for 5G millimeter wave applications. Scientific Reports, 14(1), 24086. https://doi.org/10.1038/s41598-024-75212-6

Maral, G., Bousquet, M., & Sun, Z. (2020). Satellite communications systems: Systems, techniques and technology. John Wiley & Sons.

Nabeel, M. I., Singh, K., Afzal, M. U., Thalakotuna, D. N., & Esselle, K. P. (2024). Dual-band passive beam-steering antenna technologies for low power satellite communication and modern wireless systems: A review. IEEE Access. https://doi.org/10.1109/ACCESS.2024.3400123

Phan, D. T., Palosaari, J., Kong, D., Siponkoski, T., Myllymaki, S., Leinonen, M. E., Parssinen, A., Juuti, J., & Soh, P. J. (2024). Sub-THz spatially modulated beam splitting reflectors for potential RIS implementations. 2024 18th European Conference on Antennas and Propagation (EuCAP), 1–4. https://doi.org/10.23919/EuCAP60739.2024.10501456

Pietrenko-Dabrowska, A., & Koziel, S. (2024). Variable resolution machine learning optimization of antennas using global sensitivity analysis. Scientific Reports, 14(1), 27783. https://doi.org/10.1038/s41598-024-78923-3

Pistikopoulos, E. N., & Tian, Y. (2024). Advanced modeling and optimization strategies for process synthesis. Annual Review of Chemical and Biomolecular Engineering, 15(1), 81–103. https://doi.org/10.1146/annurev-chembioeng-100522-112139

Rana, S., Sreenija, Y. S., Kumar, S., & Harish, A. R. (2024). Multi-beam passive RIS for simultaneous multi-target connectivity applications. 2024 IEEE Space, Aerospace and Defence Conference (SPACE), 741–745. https://doi.org/10.1109/SPACE63117.2024.10668921

Rosado-Sanz, J., Jarabo-Amores, M. P., Mata-Moya, D., Dauvignac, J.-Y., Lanteri, J., & Migliaccio, C. (2020). High gain sectorial beam reflectarray design for DVB-S passive radar through multi-beam optimization. 2020 23rd International Microwave and Radar Conference (MIKON), 361–366. https://doi.org/10.23919/MIKON48703.2020.9253928

Sanad, M., & Hassan, N. (2024). Performance of multibeam dual parabolic cylindrical reflector antennas in LEO satellites. IEEE Antennas and Propagation Magazine. https://doi.org/10.1109/MAP.2024.3390123

Sanyaolu, M. E., Dairo, O. F., Willoughby, A. A., & Kolawole, L. B. (2020). Estimation of rain fade durations on communication links at Ka band in equatorial and tropical regions. Telecommunications and Radio Engineering, 79(2). https://doi.org/10.1615/TelecomRadEng.v79.i2.40

Sarker, N., Podder, P., Mondal, M. R. H., Shafin, S. S., & Kamruzzaman, J. (2023). Applications of machine learning and deep learning in antenna design, optimization, and selection: A review. IEEE Access, 11, 103890–103915. https://doi.org/10.1109/ACCESS.2023.3316896

Shan, J., & Xu, X. (2024). Multipath model enhanced SBR technique for prediction of near-field EM scattering from objects on rough surfaces. IEEE Transactions on Antennas and Propagation. https://doi.org/10.1109/TAP.2024.3361234

Tan, Y. J., Zhu, C., Tan, T. C., Kumar, A., Wong, L. J., Chong, Y., & Singh, R. (2022). Self-adaptive deep reinforcement learning for THz beamforming with silicon metasurfaces in 6G communications. Optics Express, 30(15), 27763–27779. https://doi.org/10.1364/OE.460609

Tao, X., Ding, W., Wang, S., Zhang, X., Cui, W., & Cui, Q. (2024). An active multi-beam antenna design method and its application for the future 6G satellite network. Space: Science & Technology, 4, 0149. https://doi.org/10.34133/space.0149

Ullah, R., Ullah, S., Ren, J., Alwageed, H. S., Mao, Y., Qi, Z., Wang, F., Khan, S. A., & Farooq, U. (2025). Beyond fiber: Toward terahertz bandwidth in free-space optical communication. Sensors, 25(7), 2109. https://doi.org/10.3390/s25072109

Vuyyuru, S. K. R., Valkonen, R., Kwon, D.-H., & Tretyakov, S. A. (2024). Array scattering synthesis for anomalous deflection using passive aperiodic loadings. 2024 18th European Conference on Antennas and Propagation (EuCAP), 1–5. https://doi.org/10.23919/EuCAP60739.2024.10501789

Weng, C.-K., Tsai, Y.-Z., Vilenskiy, A., & Ng Mou Kehn, M. (2024). Tensor-free holographic metasurface leaky-wave multi-beam antennas with tailorable gain and polarization. Sensors, 24(8), 2422. https://doi.org/10.3390/s24082422

Xiong, R., Lu, J., Zhang, J., Liu, M., Dong, X., Mi, T., & Qiu, R. C. (2024). Design and optimization on successive RIS-assisted multi-hop wireless communications. arXiv preprint arXiv:2407.10080. https://doi.org/10.48550/arXiv.2407.10080

Xu, S., Rahmat-Samii, Y., & Gies, D. (2006). Shaped-reflector antenna designs using particle swarm optimization: An example of a direct-broadcast satellite antenna. Microwave and Optical Technology Letters, 48(7), 1341–1347. https://doi.org/10.1002/mop.21640

Zhang, W., Liu, Y., Cui, Z., Wu, C., Shi, J., Zhang, L., & Wang, S. (2025). Steerable multibeam reflector antenna for space application. IEEE Aerospace and Electronic Systems Magazine. https://doi.org/10.1109/MAES.2025.3361234

Zhou, Z. (2023). Machine learning-assisted design and analysis of electromagnetic structures [Doctoral dissertation].